CONDENSED MATTER

Origin of Magnetization in Silica-coated Fe_3O_4 Nanoparticles Revealed by Soft X-ray Magnetic Circular Dichroism

R. Dawn[1] · M. Zzaman[1,2] · F. Faizal[3,4] · C. Kiran[5] · A. Kumari[1] · R. Shahid[2] · C. Panatarani[3,4] · I. M. Joni[3,4] · V. K. Verma[6] · S. K. Sahoo[7] · K. Amemiya[8] · V. R. Singh[1]

Abstract

Magnetite (Fe_3O_4) nanoparticles (NPs) and SiO_2-coated Fe_3O_4 nanoparticles have successfully been synthesized using co-precipitation and modified Stöber methods, respectively. The samples were characterized using X-ray diffraction (XRD), Fourier transform infrared (FTIR) spectroscopy, high-resolution transmission electron microscopy (HRTEM), vibrating sample magnetometer (VSM) techniques, X-ray absorption spectroscopy (XAS), and X-ray magnetic circular dichroism (XMCD). XRD and FTIR data confirmed the structural configuration of a single-phase Fe_3O_4 and the successful formation of SiO_2-coated Fe_3O_4 NPs. XRD also confirmed that we have succeeded to synthesize nano-meter size of Fe_3O_4 NPs. HRTEM images showed the increasing thickness of SiO_2-coated Fe_3O_4 with the addition of the Tetraethyl Orthosilicate (TEOS). Room temperature VSM analysis showed the magnetic behaviour of Fe_3O_4 and its variations that occurred after SiO_2 coating. The magnetic behaviour is further authenticated by XAS spectra analysis which cleared about the existence of SiO_2 shells that have transformed the crystal as well as the local structures of the magnetite NPs. We have performed XMCD measurements, which is a powerful element-specific technique to find out the origin of magnetization in SiO_2-coated Fe_3O_4 NPs, that verified a decrease in magnetization with increasing thickness of the SiO_2 coating.

Keywords Ferromagnetic · Oxide · Spintronic · X-ray diffraction (XRD) · Transmission electron microscopy (TEM)

✉ V. R. Singh
vijayraj@cusb.ac.in

1 Department of Physics, Central University of South Bihar, Gaya-824236, India

2 Department of Physics, Jamia Millia Islamia (Central University), New Delhi 110025, India

3 Department of Physics, Universitas Padjadjaran, Jl. Raya Bandung-Sumedang Km 21, West Java, Bandung 45363, Indonesia

4 Functional Nano Powder University Centre of Excellence (FiNder U CoE), Universitas Padjadjaran, Jl. Raya Bandung-Sumedang, Km 21, West Java, Bandung 45363, Indonesia

5 Department of Animal Sciences, Central University of Kashmir, Ganderbal 191201, India

6 Department of Physics, Madanapalle Institute of Technology & Science, Madanapalle 517325, India

7 Department of Metallurgical and Materials Engineering, National Institute of Technology, Rourkela 769008, India

8 Photon Factory, IMSS, High Energy Accelerator Research Organization, Tsukuba, Ibaraki 305-0801, Japan

1 Introduction

Nanoparticles (NPs) with highly controllable magnetic properties have achieved a great aspect in biological field, mainly in diagnostic and therapeutic applications due to their nanometric size range [1–4]. Magnetic NPs (MNPs), particularly magnetite (Fe_3O_4) and maghemite (γ-Fe_2O_3), have stolen the interest of many for their outstanding performance as magnetic beads. Some incredible properties like super-paramagnetic and low toxicity have been achieved in MNPs which concludes them to various applications in biotechnological and biomedical world such as magnetic resonance imaging [1], cell sorting, enzyme immobilization [5], bio-sensing and bio-electrocatalysis [6], separation and purification of nucleic-acids from blood samples [7, 8], tumour therapy [9], and targeted drug delivery [10, 11].

To develop a high-quality magnetic Fe_3O_4 NP beads, various synthesis and characterization techniques have been explored [12–15]. As suggested by the researchers, the main requirements in MNPs are as follows: they should be chemically stable, dispersive in liquid media with a uniform size. A

protective coating becomes very essential to protect the magnetic behaviour of potentially sensitive iron ions from further environmental contamination and oxidation. In ferro-fluid, stability is preserved with the help of electrostatic interactions within the counterions and repulsive interactions among the amphoteric hydroxyl ions (H_3O^+ or OH^-). In the recent years, much effort has been devoted in the progress and betterment of silica-coated Fe_3O_4 MNPs [16–20]. For silica, the iron-oxide surface shows a strong affinity; therefore, through sol–gel process, an uncomplicated coating of amorphous silica can be occurred for such MNPs [21]. It has been found that the encapsulation of silica on the surface of iron oxide NPs can preserve their chemical stability. Such consequences of these NPs can be applied in bio-molecular field by controlling the self-assembly of nano-devices [23–25]. Molecular self-assembly highlights the core-conception of supra-molecular chemistry [26], since assembly of such molecules is proceeded by electromagnetic interactions as well as non-covalent interactions (e.g. hydrogen bonding, metal co-ordination, hydrophobic forces, van der Waals forces, electrostatic forces) and also can prevent oxidation [22]. Furthermore, the silica-coated surface may form silanol (Si–OH) group which can easily conjugate with organ-silanes by establishing Si–O-Si covalent bonds. Common illustrations incorporate the arrangement of Langmuir monolayers by surfactant molecules [27]. These strategies create a required interaction within biomolecules and materials by implementing a stable intermediate layer. To achieve a controlled spatial distribution and accumulation of crystalline magnetic nanoparticles with a controlled dimension at nanometric range, it has become a beneficial attempt through decades is by embedding or encapsulating them with a support of matrix which have the capability of keeping durably dispersed and hence limiting interparticle magnetic interactions. Such interlayers ought to accomplish satisfactory functional groups which can be associated with the biomolecules. The foremost known groups are -NH_2 (amines) that spontaneously interacts with biomolecules by developing covalent bonds [28]. Due to its significance, different biomedical applications have put a faith in developing various functionalized surfaces with advanced qualities. The functionalization of nano-shells with self-assembled monolayer (SAM) will promote nano-shell purification and can produce new prospects for nano-shell manipulation in consequent investigations with modified applications [29]. SAM-coated nanoparticles are not so interactable in air and moisture but possess a good solubility among a vast span of organic solvents. Exclusively, from the crowd of most promising coated materials, amorphous silica has achieved a high acclamation in the last decade [30–33]. In particular, magnetic interactions resulting in hardening and softening in the magnetic behaviour of the nanocomposites are greatly influenced by the concentration and dispersion of the magnetic phase within the SiO_2 matrix. To obtain small size nanoparticles have gained all interest due to its capability of behaving as a single magnetic domain in the influence of applied magnetic field without diverting their magnetic moments in different orientations and thus maximizing overall magnetization.

Encasing of the Fe_3O_4 nanoparticles in a silica coat prevents oxidation and leakage of iron ions; therefore, its inert surface can be applied for biomolecular precipitation keeping a lesser chance of irreversible binding [34]. As SiO_2 behaves as a hydrophilic layer, it becomes an important equipment to purify biomolecules [22]. For such specifications, magnetic beads have proven as one of the best tools for cell separations, like demolishing tumour cells with a great achievement in drug delivery, isolation of clouted dead cells from peripheral blood, for identifying genetic analysis of nucleic acid (deoxyribonucleic acid or DNA and ribonucleic acid or RNA) by nucleic acid separation and hence, segregation of binding proteins [7–11]. It has also proven good for protein purification by magnetic separation due to its excellent suspension ability of rapid conversion from solid-phase to solution and vice-versa with a larger binding surface area. Additionally, some of these techniques have also produced an emphasis in case of detecting nucleic acids from viruses and bacteria [8].

In this study, we have reported MNPs synthesis, a comprehensive study on their structure and a vast discussion about the magnetic characterisation of silica-coated magnetite NPs. The crystal structures have been studied by analysing the X-ray diffraction (XRD) and the chemical composite formation was observed by Fourier transform infrared spectroscopy (FTIR), whereas the detailed information about the local structure has been obtained using Fe *L*-edge and O *K*-edge by element-specific X-ray absorption spectroscopy (XAS) and X-ray magnetic circular dichroism (XMCD). The crystal morphology and the quality of coating were verified with the help of a high-resolution transmission electron microscope (HRTEM). We have performed the investigation of the effects of silica coatings with varying concentration of SiO_2 on Fe_3O_4 NPs and discussed it in the term of crystal structure as well as the local structure with the magnetic properties i.e. origin of magnetization using element-specific XMCD techniques, which consequently could give us an idea about its usefulness in biomedical applications, especially in nucleic acid separation in case of Reverse Transcription Polymerase Chain Reaction (RTPCR) techniques which have come out as one of the most authentic technique in virus detection in recent days.

2 Experimental Methods

2.1 Formation of Fe$_3$O$_4$

The MNPs in our discussion was prepared from the most commonly used co-precipitation method [34–36]. Synthesisation

from natural ironstone to Fe_3O_4 nanoparticles follows several steps as below:

In a solution, Iron (III) Chloride ($FeCl_3$) and Iron (II) Chloride ($FeCl_2 \cdot 4H_2O$, 99%) was dissolved in a 2:1 molar ratio and treated with deionized water in a magnetic stirrer before heating it up to reflux. These are stirred for 1 h at 500 rpm. Then, after 1 h, the addition of Polyethylene glycol (PEG) 6000 was stirred little by little into the Fe mixture and stirred for 1 h at 500 rpm. Ammonia solution (NH_4OH) is mixed with PEG 6000 and again stirred for 1 h at 500 rpm once the mixture reaches to 70 °C. This process forms a black precipitation which was washed by deionized water for several times and further separated by using centrifugation. Therefore, the Fe_3O_4 synthesisation process occurs through the following reaction:
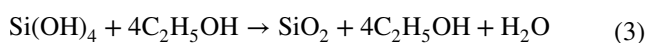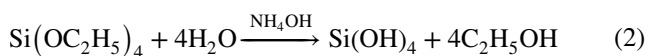
$$2FECl_3 + FeCl_2 + 8NH_4OH + H_2O \rightarrow Fe_3O_4 + 8NH_4Cl + 5H_2O \quad (1)$$
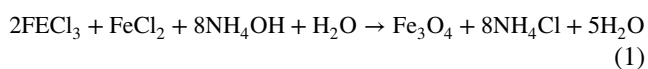
After this synthesis, $FeCl_3$ and $FeCl_2$ are mixed by dripping $FeCl_3$ into $FeCl_2$ using a micro pump with speed controller 8 with stirring at 500 rpm. (a black precipitate of Fe_3O_4) is formed.

After the running out of $FeCl_3$, drip into the $FeCl_2$ is dripped into it and then supplied N_2 gas into the solution for 1 h with N_2 gas flow rate of 0.8-1L/min while stirring at 500 rpm. After giving N_2 gas into the sample solution, wash the formed Fe_3O_4 sample to a neutral pH (pH 7) using Aquadest. Fe_3O_4 samples that have been washed until neutral (pH 7), the Fe_3O_4 samples are dispersed with ethanol and the coating reaction was immediately started to prevent the oxidation.

2.2 Formation of Si + Fe_3O_4

Encasing of silica on Fe_3O_4 MNPs was synthesized by modified Stöber method [37, 38]. This preparation follows a sol–gel method to synthesize SiO_2 particles using Tetraethyl Orthosilicate (TEOS) in addition with surface-active molecules as precursors using a micro pump speed controller 8, stir at 500 rpm. The reaction process is as follows:

$$Si(OC_2H_5)_4 + 4H_2O \xrightarrow{NH_4OH} Si(OH)_4 + 4C_2H_5OH \quad (2)$$

$$Si(OH)_4 + 4C_2H_5OH \rightarrow SiO_2 + 4C_2H_5OH + H_2O \quad (3)$$

In this reaction procedure, ethanol and Ethoxysilanos ($Si(OH)_4$) condenses by releasing water. In this way, the synthesis parameter helps SiO_2 to encase the surface-active molecules. Those surface-active molecules vanish via the heating process and hence create empty pores and form hollow particles of silica. Subsequently, the silica/Fe_3O_4 attaches and permits the formation of core–shell structures. NH_4OH and deionized water have been mixed into the Fe_3O_4 and

TEOS mixture using a micro pump speed controller 8, stir at 500 rpm for 1 h. After 1 h of stirring, the sample solution is washed using ethanol until pH 7 is achieved. The sample is then re-dispersed with ethanol. The samples were dried in a drying oven at a temperature of 60 °C for 12 h.

We have produced different concentrations of Si-encapsulated Fe_3O_4 nanoparticles by differing the proportions of TEOS with Fe (II) and Fe (III) precursors. We have measured their actions with respect to the non-capsulated Fe_3O_4 nanoparticles. We have tried to recognize them by mentioning Fe_3O_4@SiO_2: 0 (for non-capsulated Fe_3O_4), Fe_3O_4@SiO_2: 1 (for 71.875 g/ml capsulation coating), Fe_3O_4@SiO_2: 2 (for 107.812 g/ml capsulation coating), Fe_3O_4@SiO_2: 3 (for 143.750 g/ml capsulation coating), Fe_3O_4@SiO_2: 4 (for 215.625 g/ml capsulation coating), Fe_3O_4@SiO_2: 5 (for 287.5 g/ml capsulation coating) and hereafter referred as S.0, S.1, S.2, S.3, S.4, and S.5 respectively.

2.3 Characterizations

The samples were probed by X-ray diffraction (XRD) (Rigaku X-Ray Diffractometer) using a Cu K_α ($\lambda = 1.540$ Å) with angular resolution of step-size 0.001° having θ–2θ range 10–90° and generator setting on 40 kV and 40 mA. The average size of the nanoparticles was determined from full-width at half maxima (β) and the Bragg angle (θ) of the reflection [311] using Scherrer's equation [39] :

$$D = k\,\lambda/\beta\,\cos\theta \quad (4)$$

where D refers to the mean diameter of the crystalline domain of the particles, k is the constant proportionality parameter (assumed $k = 0.9$), and λ is the wavelength of X-ray radiation. The infrared (IR) spectra of the sample were measured using IR Spectroscopy through Fourier transform (FT-IR) technique of Nicolet 6700 spectrometer, Thermo Scientific, arranged with DTGS detector, (preparing a mixture to dilute the sample in KBr 1%) at a range of 4000 to 500 cm^{-1} having 4 cm^{-1} resolutions in 128 acquisitions. The elemental analysis was done by Shimadzu X-ray fluorescence spectrometer (model EDX 720). The samples were kept inside the sample holder with the help of a polypropylene film and the Si and Fe content were calculated by the Quali Quant method, which was supplied by Shimadzu. We have also used HRTEM 9500 (Hitachi) with LaB6 as a source of electron at 300 kV to study the size and morphology of the nanoparticle samples and their compositions. For the preparation of sample, the nanoparticles were diffused in ethyl alcohol by ultrasonic bath followed by a deposition on the TEM copper grid of 400 mesh, packed with carbon and then dehydrated at room temperature. To study the size of the nano-particles, we have plotted the linear function graphs of frequency (counts) vs particle size (nm) with the help of particle size analyzer (PSA) technique corresponding with various TEM measurements. The magnetic

properties were measured by vibrating sample magnetometer (VSM) (ADE, EV-7VSM, USA), X-ray absorption spectroscopy (XAS) and X-ray magnetic circular dichroism (XMCD) measurements at a Beamline of BL-16A, Photon Factory, High Energy Accelerator Research Organisation (KEK-PF, Japan). The monochromator having resolution $E/\Delta E \geq 5000$ with circular polarization at $87\% \pm 4\%$ [40]. The vacuum chamber sustains a pressure at 1×10^{-9} Torr. We have performed the XAS measurements in total electron yield (TEY) mode occurring the probing depth at ~ 5–10 nm [41].

3 Results and Discussions

3.1 Structural and Elemental Characterization

Figure 1 shows the XRD patterns of Fe_3O_4 MNPs, which is in good concurrence with the crystal-structure pattern of magnetite. The characteristic peaks can be recognized at 2θ positions = 18.01° (111), 30.284° (220), 35.662° (311), 43.289° (400), 53.5° (422), 57.173° (511), 62.844° (440), 71.351° (151), and 74.284° (002). The patterns of S.0 and S.3 are shown in Fig. 1 as an example. The XRD pattern of magnetite (PDF No. 96–900-7645) is included in the figure
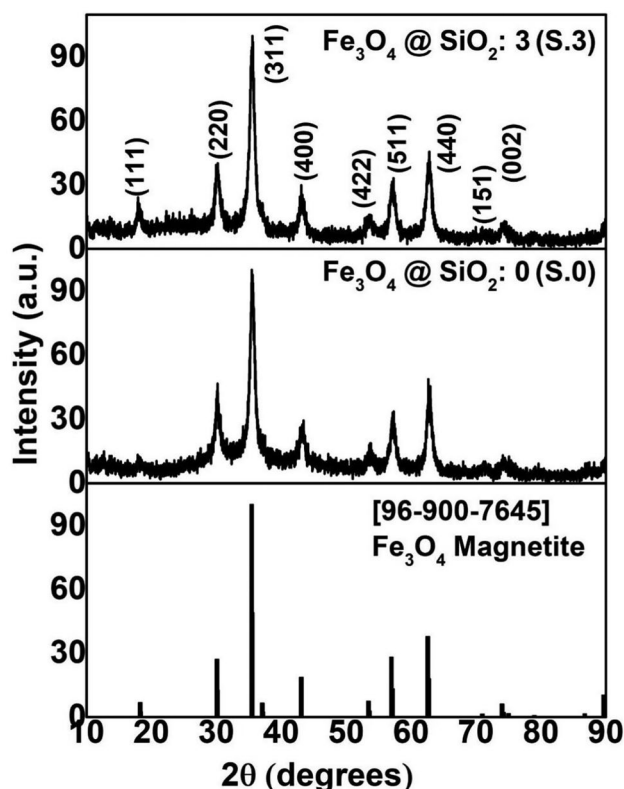
for comparison. Both S.0 and S.3 showed identical XRD pattern, with a small change in background in sample S.3. This may be due to the presence of amorphous SiO_2 in the sample. The intensity of (111) peak is weak in S.0 sample; it could be due to small signal-to-noise ratio. Moreover, the crystallinity was found to be the same having only a little change in the characteristic peaks' intensity, due to the presence of amorphous silica. We have determined the mean diameter of sample S.0 and S.3 using Rietveld analysis and Scherrer's equation, which had come out to be about 6 ± 1 nm and 7 ± 2 nm, respectively corresponding to the {311} plane. We have also confirmed the reproducibility of the XRD patterns in the terms of peaks, peak position, and average particle size on another set of synthesized MNPs. Thus, the XRD data suggest that MNPs obtained in the present study has size distributions in nano-meter size.

The absorption infrared spectra lie in the wavenumber ranging from 4000 to 500 cm^{-1} of samples S.0 and S.3 are shown in Fig. 2. The results of IR absorption peaks indicate the types of functional group of Fe_3O_4 NPs and $SiO_2@Fe_3O_4$ present in NPs. The O–H bond was found in the range of 3550–3000 cm^{-1}, whereas the H–O–H acquired a symmetric bending at ~ 1630 cm^{-1}. Therefore, the bands ranging from 1600 to 3500 cm^{-1} can be considered the H–O-H stretching modes and bending vibration of the free or water-absorbed conditions. The Fe–O-Si band arrived at ~ 1050 cm^{-1} proves that the sample has a proper SiO_2 doping [42–45]. At the wavenumber ~ 570 cm^{-1}, Fe–O showed an asymmetric vibration [42]. This supports the XRD data which showed that SiO_2-coated Fe_3O_4 NPs have been formed. Here, we would like to remind you that this study area focuses about the synthesize of silica-coated Fe_3O_4 NPs not silica-disperse Fe_3O_4. To form the coating by Stöber approach, parameters should

Fig. 1 (Colour online): XRD patterns of S.0 and S.3 samples compared with the magnetite (JCPDS no.- 96–900-7645)
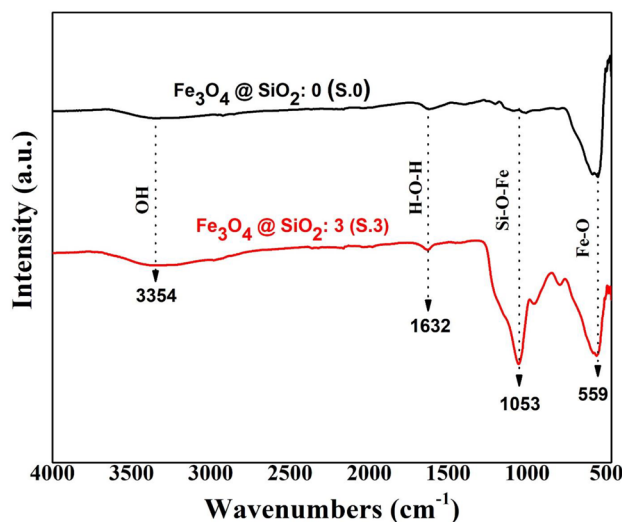
Fig. 2 (Colour online): FTIR spectra of S.0 and S.3 samples

be optimised during synthesis of NPs. In fact, the silica condensation rate must be quicker than its hydrolysis. The condensation rate of silica could be regulated by using low pH, low concentration of TEOS, and low synthesis temperature.

Elemental analysis was done by using EDX analysis which is presented in the graphical abstract. We calculated the average composition of samples S.0 and S.3 with an electron probe which covers hundreds of particles and thus, confirming the composition. From the analysis, it is clear that as the concentration of TEOS increased, the amount of silica will also increase. The EDX results also confirmed that synthesis procedures are completely reproducible with a nice synthesizable capability for both of the pure and Si-encapsulated MNPs. Despite the hydrophilicity of NPs in Fe_3O_4, there is a chance for aggregation among the particles due to their nominal size and thus demands to decrease the surface energy. In the synthesis process no any surfactant was used, this aggregation was quite expected as stated in the literature [21, 46, 47].

3.2 Transmission Electron Microscopy

All the particles prepared got almost a spherical approach with a regular average size as shown by transmission electron microscopy (TEM) images in Fig. 3. Here, we assumed that N particles have been used in order to determine the particle sizes for S.0 and S.3 samples from TEM images; histogram has been mounted (not shown here) followed by Sturges's method [48]. For fitting histogram, we adopted lognormal distribution function as

$$f(\sigma) = \frac{1}{\sqrt{2\pi}\delta D} \exp\left(-\ln^2\left(\frac{\sigma/\sigma_0}{\delta^2}\right)\right) \tag{5}$$

where σ_0 is the average value and δ is the poly-dispersion index. The average NPs size can be determined using expression as

$$\sigma_{avg} = \sigma_0 \exp\left(\frac{\delta^2}{2}\right) \tag{6}$$

The average diameter of 7.1 nm and 8.5 nm for S.0 and S.3 samples was observed which are consistent with XRD as shown in Table 1.

3.3 Magnetic Characterization

3.3.1 Vibrating Sample Magnetometry (VSM)

The magnetization of S.0 and S.3 samples in the range of ± 1 T is shown in Fig. 4 introducing as functions of magnetic field. The hysteresis loops of these samples confirm the ferrimagnetic behaviour which originates only from Fe_3O_4 NPs (where Fe^{3+} ions are located at the tetrahedral (T_d) and also in the octahedral (O_h) sites having a ratio 1:1 and Fe^{2+} ions are also located at the O_h sites) as because SiO_2 is non-magnetic. Therefore, Fe^{2+} ions at O_h sites are responsible to produce net magnetization while Fe^{3+} ions at O_h and T_d sites will cancel each other and will not contribute to net magnetization [49].

Fig. 3 (Colour online): HRTEM images of samples: (**a**), (**b**) S.0 and (**c**), (**d**) S.3, histogram fitted with lognormal function are shown in the insets of (**a**) and (**c**) for S.0 and S.3, respectively
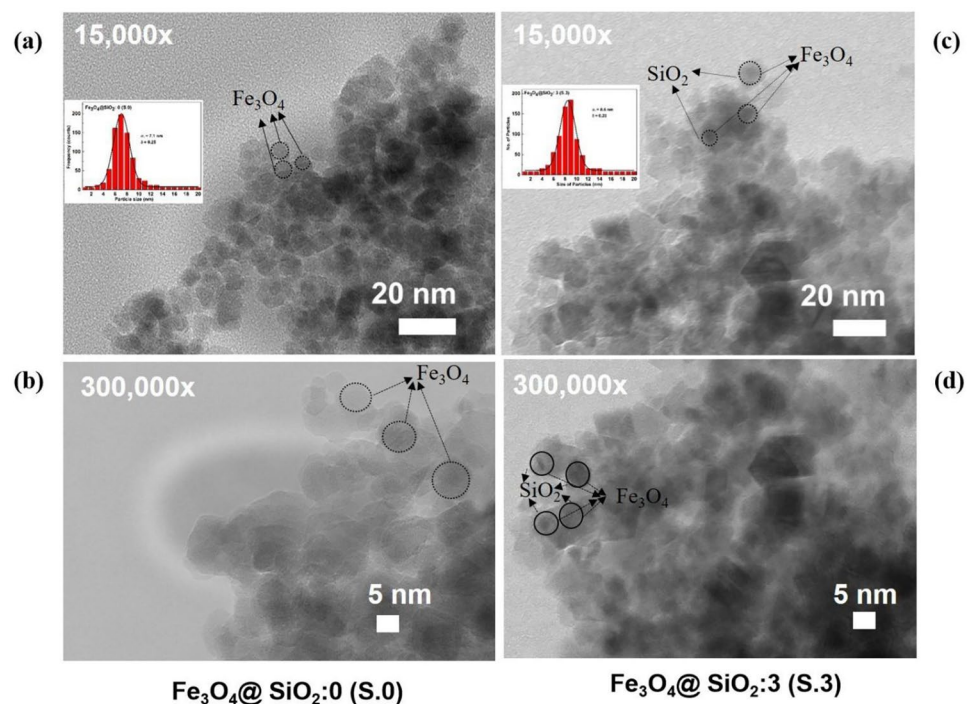
Table 1 Particle size, SiO$_2$ thickness, and saturation magnetization

Sample name	TEOS (gram/ml)	Size of crystal (nm)	Thickness of SiO$_2$ (nm)	Total size of crystal@ SiO$_2$ (nm)	Magnetization (emu/g)
S.0	0	6 ± 1	0	6.0 ± 1	62.31
S.1	71.88	6 ± 1	1	7.0 ± 1	52.12
S.2	107.81	6 ± 1	1.4	7.4 ± 1	32.32
S.3	143.75	6 ± 1	2.0	8.0 ± 1	21.86
S.4	215.63	6 ± 1	2.6	8.6 ± 1	15.26
S.5	287.50	6 ± 1	3.2	9.2 ± 1	9.13

Using Bloch theory [50], the demagnetization can be described as:

$$M(T = T) = M(T = 0)\left[1 - \xi ST^{3/2}\right] \qquad (7)$$

Here, $M(T = T)$ and $M(T = 0)$ define magnetization at $T = T$ K and 0 K respectively; ξ is surface thickness; S is stiffness constant of spin-wave referring T as temperature. Thus, at a specific temperature, the magnetization will vary with respect to ξ and S. As the concentration of SiO$_2$ increases, the value of ξ increases [51]. Therefore, the magnetization decreased as the coating of SiO$_2$ on Fe$_3$O$_4$ increases as shown in Table 1. Thickness of SiO$_2$ coating is reducing the interaction of the intrinsic magnetic moment of Fe$_3$O$_4$ MNPs with the externally applied magnetic-fields. Zhao et al. [52] mentioned the reduction of magnetization due to weight contribution of SiO$_2$. However, the other possibility should be SiO$_2$ passivation and their strong impact in the suppression of magnetization. Coskun and Korkmaz [53] stated that the SiO$_2$ passivated the nanoparticle and due to passivation, the magnetic interaction between nanoparticles decreases which results the reduction in magnetization. The saturation magnetization of the S.0 and S.3 samples was 62.31 emu/gm and 21.86 emu/gm, respectively with coercivity ~ 196 Oe in both samples as shown in the inset of Fig. 4 unlike Kralj et al.

[35], which confirms that MNPs are not in a superparamagnetic state. This result gets a reliability about the presence of spontaneous exchange bias through the hysteresis loops in the samples which indicates the reduction of the number of available magnetic moments and thus negatively affects the net magnetization in the samples [54]. To proceed further investigation, we adopted element-specific and powerful techniques i.e., XAS and XMCD and performed to find out a microscopic origin of magnetizations in Fe$_3$O$_4$ along with SiO$_2$-coated Fe$_3$O$_4$ NPs.

3.3.2 X-ray Magnetic Circular Dichroism

We used the X-ray magnetic circular dichroism (XMCD) technique in order to get spin and orbital magnetic moments. Unlike magnetometry, XMCD is powerful element-specific technique and proficient to extract separately spin and orbital magnetic moments. Using sum rules, one can obtain orbital and spin contributions in total magnetization. The XAS measurements were carried out on all the samples i.e., from S.0 to S.5. A magnetic field along the parallel direction to the beam and consequently perpendicular to membranes was applied in the range of ± 3 T at 300 K. The XAS was first recorded by scanning the energy across the Fe $L_{2,3}$ edges, from 690 to 730 eV. The $L_{2,3}$ edges of Fe 2p core level split the XAS into L_3 (2p$_{3/2}$) and L_2 (2p$_{1/2}$) edges due to spin–orbit coupling and both the edges separated by ~ 13 eV. The L_3 and L_2 edge spectra arise due to spin–orbit interaction of the 2p core shell. The magnetic moment of the element is proportional to the number of the empty valence state of 3d shell. In order to rule out the background slope contribution which arises due to charge absorption at the $L_{3,2}$ absorption edge peak, i.e., below L_3 to above L_2 edges, the XAS absorption spectra were carefully normalized to 1. In Fig. 5, μ^+ and μ^- denote the absorption coefficients for photon helicity parallel and antiparallel to the majority spin direction of Fe, respectively. The XMCD spectrum is obtained by taking the difference between two opposite helicities of XAS spectra measured at particular magnetic field i.e. $\Delta\mu = \mu^+ - \mu^-$. The XAS and XMCD spectra of Fe$_3$O$_4$ and SiO$_2$-coated Fe$_3$O$_4$ MNPs sample showed fine or multiplet structures which are characteristic of the localized 3d state of Fe as shown
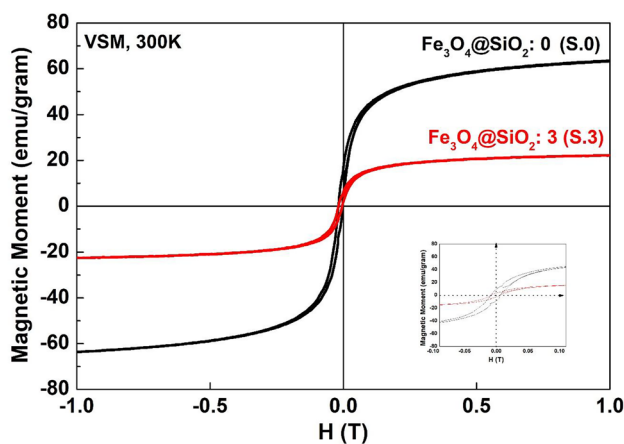

Fig. 4 (Colour online): Hysteresis loop of S.0 and S.3 samples

in Fig. 5. The Fe L_3-edge XMCD spectra have a positive peak at 708.0 eV, where Fe^{3+} is at tetrahedral (T_d) site and two negative peaks at 706.8 eV, where Fe^{2+} is at octahedral (O_h) sites and 708.7 eV, where Fe^{3+} is at O_h sites. The XAS and XMCD spectra of all MNPs are compared with those of other Fe compounds as shown in Fig. 5(c, d). The line shape of the Fe $L_{2,3}$ XAS and XMCD spectrum of Fe_3O_4 NPs was not similar from line shape that is found in Fe metal [55], which indicates the absence of Fe metal segregation in Fe_3O_4 NPs. However, the line shape of Fe $L_{2,3}$ XAS and

XMCD spectrum of Fe_3O_4 NPs closely resembles with both the Fe_3O_4 (Fe^{3+}: Fe^{2+} =2:1) [56] and γ-Fe_2O_3 (Fe^{3+}) [56], specifying the fact that Fe ions in Fe_3O_4 NPs have valency of 2 + and 3 + both. In Fe_3O_4, the Fe^{2+} (O_h) peak is large compare to Fe^{3+} (O_h) peak while in Fe_3O_4 NPs, we found that the Fe^{2+} (O_h) peak was significantly less compare to Fe^{3+} (O_h) peak. This arises from the fact that in the octahedral sites of Fe_3O_4 NPs, Fe^{2+} ions possess limited occupancy. The same reason of occupancy refers to the existence of secondary γ-Fe_2O_3 phase or vacancy of Fe that leads to a

Fig. 5 (Colour online): (**a**) XAS and (**b**) XMCD Spectra of samples S.0–S.5 showing Fe L-edge; (**c**) XAS spectra compared with XAS patterns of γ-Fe_2O_3 [52], Fe_3O_4 [52], pure Fe [51]. (**d**) XMCD spectra compared with XMCD patterns of γ-Fe_2O_3 [52], Fe_3O_4 [52], and pure Fe [51]
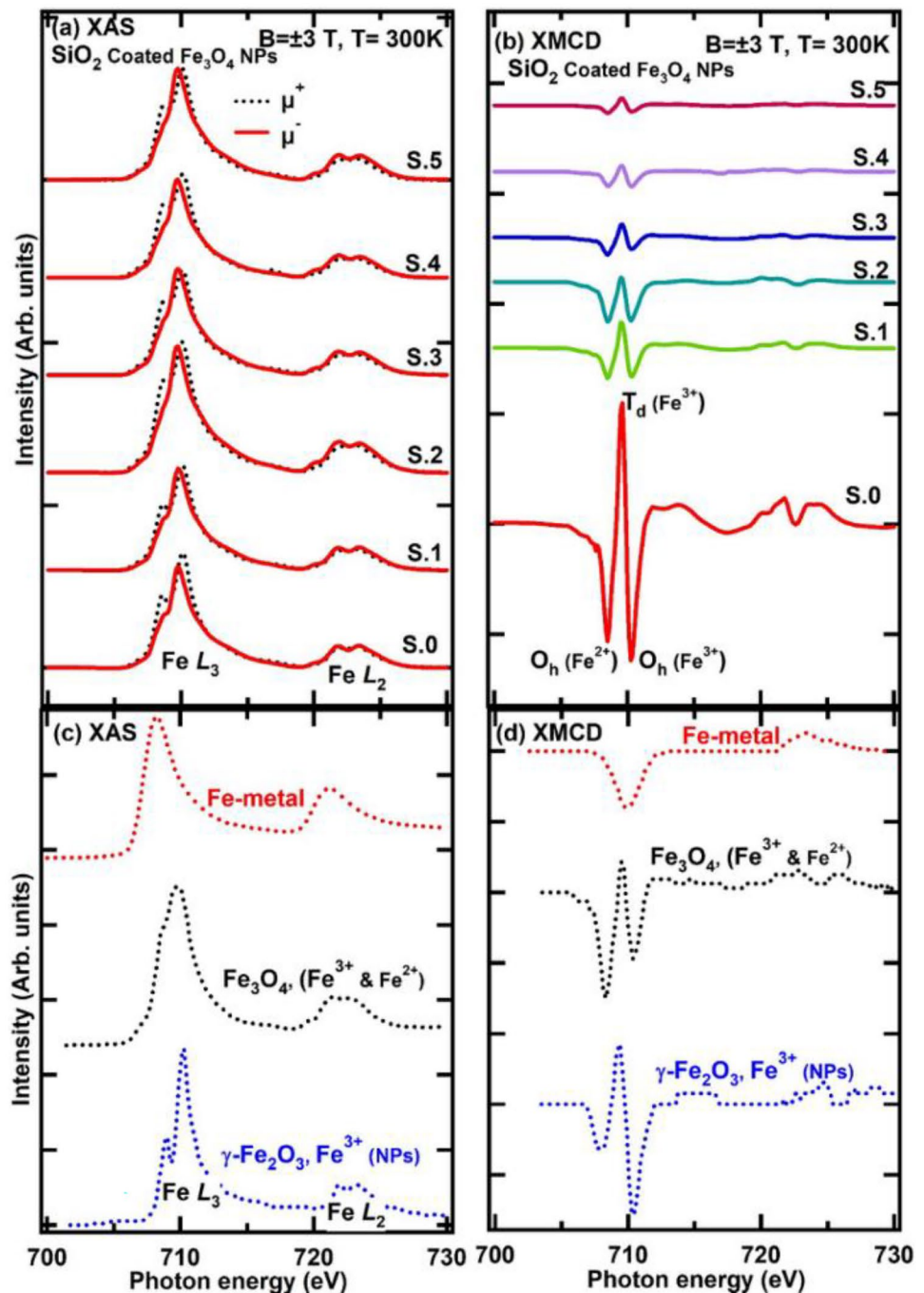
non-stoichiometric $Fe_{3-\delta}O_4$ in case of Fe_3O_4 NPs. Following SiO_2 coating, the ratio of intensity in Fe^{2+} (O_h) increases suggesting that Fe^{2+} ions at octahedral sites have increased and hence it forms stoichiometric Fe_3O_4. However, SEM and TEM techniques verify the existence of Fe_3O_4 phase, ruling out the occurrence of additional Fe-oxide phases. According to Pellegrin et al., the increased intensity of Fe^{3+} (O_h) ions is due to the nonstoichiometric $Fe_{3-\delta}O_4$ rather than γ-Fe_2O_3 [57]. Ho et al. have shown in their report that the shape-dependent occupancy of the cations present in the O_h sites was mostly occupied by Fe^{3+} ions when Fe_3O_4 NPs has cubic shape rather than polyhedral [58].

The orbital magnetic moment (m_{orb}) along with the spin magnetic moment (m_{spin}) of Fe_3O_4 and SiO_2-coated Fe_3O_4 NPs was determined using sum rules [59–66] on the integrated XMCD and total XAS spectra of Fe $L_{2,3}$ edges based on equation:

$$m_{orb} = \frac{-4q}{3r} n_h \mu_B \qquad (8)$$

$$m_{spin} = -2 \frac{[3p - 2q]}{r} n_h \mu_B - 7m_T \qquad (9)$$

The integrated spectra of XAS and XMCD provide the parameters (p, q, and r) for the sum rule to obtain the m_{orb} and m_{spin}, indicating p as the integral value of L_3-edge, q being the integral for both of the L_2 and L_3-edges of XMCD and r refers to the integral of the sum of XAS possessing two helicities of light; n_h signifies the number of holes in the 3d orbital of the transition metal used here and lastly m_T defines the magnetic quadrupole moment. We take consideration of $n_h = 13.7$ for Fe^{3+} ion [67]. According to the measurements of Fe 2p core level photoemission [68], the net numbers of 3d electrons of Fe^{3+} and Fe^{2+} are 5.3 and 6.1, respectively. The calculated numbers of electrons in 3d bands are 16.7 electrons per formula unit of Fe_3O_4. In addition, the LDA + U calculations show that the number of 3d electrons in Fe_3O_4 is 16.32. Therefore, the number of holes, $n_h = 13.7$ per formula unit of Fe_3O_4 in the 3d band [69].

To eliminate the non-magnetic part from the spectra of XAS, a step-function having an arc-tangent base was used for threshold fitting. The non-magnetic portion was < 1/1000 times from the total absorption in the raw data. The saturation effect was approximately ~ 2% at the normal incidence in our case. The magnetic-dipole becomes inconsiderable for the cubic symmetry in magnetite, even though it breaks the additional surface symmetry [60]. The determined value of m_{spin}, m_{orb}, and m_{orb}/m_{spin} vs field for S.0–S.5 samples is plotted in Fig. 6. The magnetic moment decreased in SiO_2-coated Fe_3O_4 NPs compared to the Fe_3O_4 NPs. After the encapsulation of silica, the 3d orbitals of the Fe ions at the octahedral sites occur splitting which results to a gradual
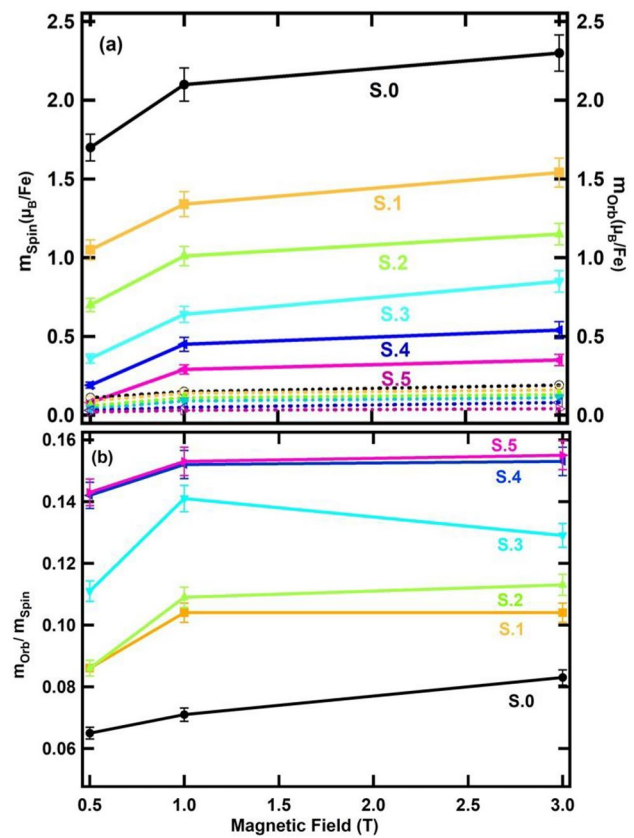

Fig. 6 (Colour online): (a) The m_{spin} and m_{orb} (b) m_{orb}/m_{spin} vs magnetic field of samples S.0–S.5. Solid lines represent m_{spin} and dotted lines represent m_{orb}

decrement in their magnetic moment. Those 3d orbitals at O_h sites split into lower t_{2g} (d_{xy}, d_{xz}, and d_{yz}) and higher e_g (d_{z^2} and $d_{x^2-y^2}$) energy levels. The crystal field splitting in the tetrahedral field (Δ_t) is quite smaller than the crystal field splitting in the octahedral field ($\Delta_o = 2.25\Delta_t$). Hence, pairing of electrons in octahedral field is larger compare to tetrahedral field. In SiO_2-coated Fe_3O_4 NPs, the Fe^{2+} ions present in the O_h sites are increased. The electrons in Fe^{2+} ions at octahedral site first occupies lower t_{2g} levels and then forward for higher e_g levels resulting in the formation of more pairs of electrons. X. Che and H.N. Bertram explained that with the increase of nonmagnetic layer, the ferromagnetic exchange coupling decreases and the interaction between the two magnetic layers couple anti-ferromagnetically which reduces the magnetization [70]. Thus, a deduction in the magnetic moment is found here for samples S.1-S.5. According to Mendonça et al., SiO_2 coating enlarges the paramagnetic component and concludes to a decrement of magnetic moment [71]. Interestingly, such trend of M_r and M_s values in the M-H loop occurred from the VSM measurement were establishing a similar pattern with S.0 and S.3 samples but slightly higher. This discrepancy comes in

play as the value of magnetic moment determined from the experimental XMCD spectra belongs to the surface region as proposed by Amemiya et al. [72]. In XMCD measurement, the probing depth was chosen in the range of ~5 nm as the TEY mode was only depicted in our experimental section. The Fe_3O_4 NPs coated by amorphous SiO_2 affect the signal so the majority of the signals arriving from these topmost surface layers are supressed. From XRD and TEM images, it is also seen that SiO_2 layers (1–2 nm) are present at the surface of Fe_3O_4 NPs. These are not probed by the XMCD spectra in TEY mode, although the values of M_r and M_s occurred from the M-H loop also contribute from the total volume of the NPs.

The measurement of O K-edge XAS was performed at 300 K to discriminate Fe_3O_4 from γ-Fe_2O_3. Figure 7 represents normalized spectral formation of O K-edge XAS of S.0–S.5 MNPs samples. The features labelled with A, B, and C are similar to XAS data of Fe_3O_4 published previously [73–76]. The spectral features labelled with A in the pre-edge region (below 535 eV) specify transition from the unoccupied O $1s$ state to hybridized states of O $2p$–Fe $3d$, preferring most of the localization in the Fe-site. From XAS spectrum, it has been proven that the pre-peak of the Fe_3O_4 NPs split into two peaks where A_1 with energy value 530.4 eV specifies the t_{2g} state having π characteristics, whereas A_2 (the shoulder peak) at 531.5 eV specifies e_g state having σ characteristic followed from ligand field theory. The B and C features found in the post-edge

region (above 535 eV) refer to the transitions of electrons from O $1s$ to O $2p$ states which follows their hybridization states at Fe $4s$ and $4p$, respectively. The splitting of energy and relative intensities of peaks A_1 and A_2 were functions of the O-Fe structure. The splitting between A_1 and A_2 has a larger energy value in α-Fe_2O_3 (1.45 eV) and occurs a reduction to 1.05 eV for Fe_3O_4 and γ-Fe_2O_3, although a spectral shift in the absorption edge at -0.35 eV for all the features of γ-Fe_2O_3 and Fe_3O_4 is exhibited which signifies a shift towards lower energies [72, 74]. In addition, with such observations, a relative intensity of the peaks A and B, i.e., I_A/I_B that determines the population density of holes in $3d$ band is further compared with the hole population of $4sp$ band. The spectra were fitted by Gaussian function using *IgorPro* which provided the accurate values of peak positions, intensities along with the accurate measured areas within the peaks. The intensity of peaks A_1 and A_2 spectra in pre-edge region of O K-edge clearly decreased for SiO_2-coated Fe_3O_4 MNPs. Similarly, the intensity of XMCD of Fe L_3 edge decreased for SiO_2-coated Fe_3O_4 MNPs. These results indicated that the SiO_2 were uniformly dispersed over the surface of Fe_3O_4 NPs. Because of uniform distribution of SiO_2 over Fe_3O_4 NPs, the probing depth capacity decreases and the intensity of O K-edge and Fe L_3-edge of XMCD suppressed. Figure 7 provides the evidence that there were no significant shifts found in the spectra of Fe_3O_4 NPs with respect to SiO_2-coated Fe_3O_4 MNPs except a decrement in the t_{2g}/e_g intensity ratio that signifies the changes occurred at

Fig. 7 (Colour online) O K-edge XAS spectra of Fe_3O_4 (sample S.0) and SiO_2-coated Fe_3O_4 NPs (samples S.1–S.5)
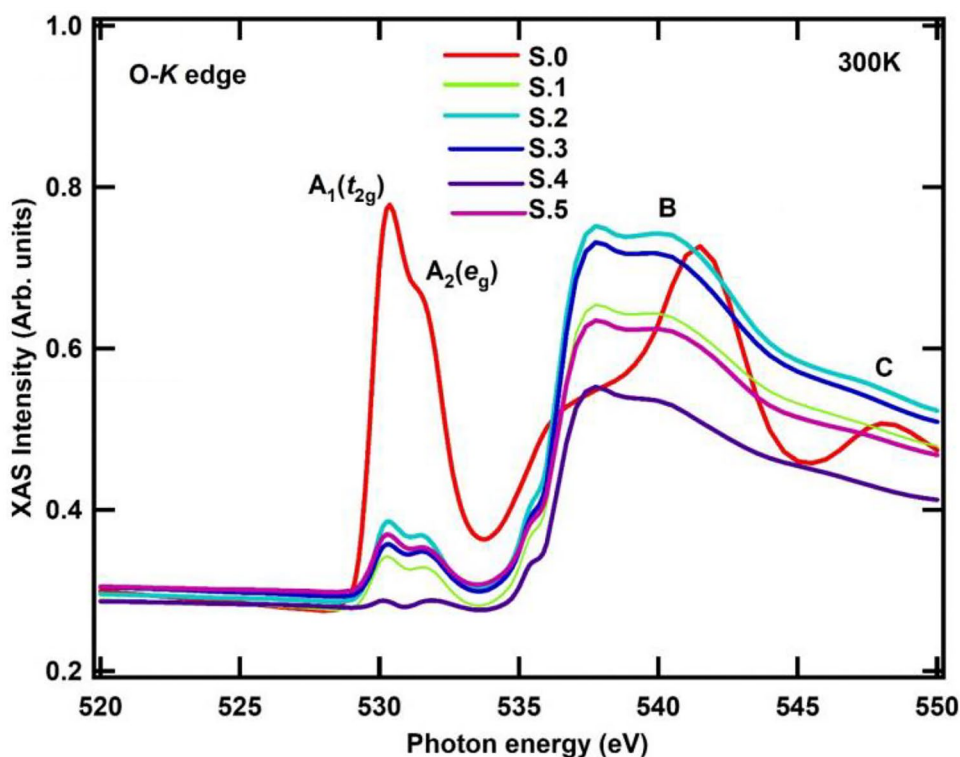
the local environment. The intensity ratio I_A/I_B is also found to be increased in SiO_2-coated Fe_3O_4 MNPs compared to Fe_3O_4 due to the increment of the population of holes in the $3d$ band as verified with hole-population of the $4sp$ band in SiO_2-coated Fe_3O_4 MNPs.

Coming to an end, it becomes worth analysing that the potential of the synthesized SiO_2-coated Fe_3O_4 MNPs which have been used for various biological applications. By utilizing the advantages of magnetic property, high surface area due to nanoparticle, good dispersion, and easy separation of MNPs in buffer systems, the nucleic acid of other pathogenic viruses infected in blood can be separated. From our preliminary data, NPs size distributions are smaller compared to the commercial one which is enhancing the performance of the DNA (or, nucleic acid) separation and are under progress to help the hospitals or the medical field in RTPCR diagnosis for COVID-19.

4 Conclusion

The single-phase Fe_3O_4 NPs and silica-coated Fe_3O_4 NPs were prepared by co-precipitation of Fe (III) and Fe (II) precursors with 2:1 ratio, using modified Stöber methods, respectively. XRD verification showed that reproducible materials gather high proximity between the crystalline size domains in case of MNPs. It is also confirmed that we were able to make nano-size Fe_3O_4 NPs. From the spectral demonstration of FT-IR, it is verified that the surface of the magnetite achieved a successful capsulation of silica. HRTEM images exhibited that most of the MNPs have an approximately spherical shape and a mean regular diameter. The same spherical distribution along with a perfect distribution of encapsulated NPs was found for silica-coated Fe_3O_4. The magnetic properties of the NPs and their origin were confirmed by the measurements of magnetization. After the encapsulation of SiO_2 on Fe_3O_4 NPs, an interface of Si–O–Fe gets generated which is confirmed from FTIR results. This distribution of Si–O–Fe layer has an immense emphasis in changing the net magnetization of the NPs. Due to the presence of non-magnetic SiO_2-layer, Fe_3O_4 shows a striking change in its magnetic properties. Fe_3O_4 with inverse spinel structure exhibits double exchange ferromagnetic interaction in its bulk, while at the surface region, Fe^{2+} ions at O_h-sites and the Fe^{3+} ions occupying the T_d-sites have an antiparallel arrangement of magnetic moments. Hence, there exists an antiferromagnetic superexchange interaction creating anti-phase boundary. The presence of non-magnetic SiO_2 reduces the phase boundary and enhances the anti-ferromagnetic property at the Si–O–Fe interface. Hence, the ferromagnetic exchange coupling decreases monotonically with the increase in the interlayer thickness. X. Che and H.N. Bertram support that

a magnetic material consists of many small single-domain grains [70]. Each grain has uniaxial anisotropy due to either stress, shape of the particle and the crystal structure. The increment of the ratio of Fe^{2+} ions at the octahedral site in the XMCD analysis also gives an emphasis to this fact. The surface defect generated at the interlayer region of the coated Fe_3O_4 NPs can break the superexchange paths due to the increasing thickness of SiO_2 and induce spin disorder that leads to less magnetization with paramagnetic behaviour in nanocrystalline $SiO_2@Fe_3O_4$. The net saturation magnetization decreased as the amount of silica increased on the Fe_3O_4 NPs. XMCD measurements suggested that SiO_2 coating increased the paramagnetic component which resulted to a gradual decrement of the magnetic moments. Such reduction in the magnetic moment after silica coating could be related to the fact that the $3d$ orbitals of Fe ions occur splitting at O_h sites. The O K-edge XAS spectra suggested that there were no specific shifts found along the spectra of Fe_3O_4 NPs compared to SiO_2-coated Fe_3O_4 MNPs except for the decrease in the intensity ratio of t_{2g}/e_g which was occurred for the change in a local environment.

Author Contribution R. Dawn: methodology, investigation, formal analysis, writing—original draft, review and editing. M. Zzaman: investigation, validation. F. Faisal: investigation and formal analysis, validation. C. Kiran: conceptualization, investigation, validation. A. Kumari: validation. R. Shahid: investigation and formal analysis, validation. C. Panatarani: investigation and formal analysis, validation. I. M. Joni: investigation and formal analysis, validation, funding acquisition. V.K. Verma: investigation and formal analysis, validation. S. K. Sahoo: formal analysis, review and editing. K. Amemiya: formal analysis, review and editing. V. R. Singh: conceptualization, formal analysis, review and editing, supervision, funding acquisition.

Data Availability The data that support the findings of this study are available from the corresponding author upon reasonable request.

Declarations

Conflict of Interest The authors declare no competing interests.

References

1. H. Fatima, K.S. Kim, Adv. Powder Technol. **29**, 2678 (2018)
2. M.H. Mashhadizadeh, R.P. Talemi, Mats. Sci. and Engg. C. **59**, 773–781 (2016)

3. S. Ni, X. Sun, X. Wang, G. Zhou, F. Yang, J. Wang, D. He, Mater. Chem. Phys. **124**, 353 (2010)

4. Z.W. Li, Z.H. Yang, J. Magn. Magn. Mater. **387**, 131 (2015)

5. K.E. McCloskey, J.J. Chalmers, M. Zborowski, Anal. Chem. **75**, 6868 (2003)

6. R. De Palma, C.X. Liu, F. Barbagini, G. Reekmans, K. Bonroy, W. Laureyn, G. Borghs, G. Maes, J. Phys. Chem. C. **111**, 12227 (2007)

7. H.Y. Park, M.J. Schadt, L.Y. Wang, I.I.S. Lim, P.N. Njoki, S.H. Kim, M.Y. Jang, J. Luo, C.J. Zhong, Langmuir **23**, 9050–9056 (2007)

8. X.Q. Xu, C.H. Deng, M.X. Gao, W.J. Yu, P.Y. Yang, X.M. Zhang, Adv. Mater. **18**, 3289–3293 (2006)

9. S. Kayal, R.V. Ramanujan, Mater. Sci. Eng. C **30**, 484–490 (2010)

10. C.L. Huang, W.J. Hsieh, C.W. Lin, H.W. Yang, C.K. Wang, Ceram. Int. **44**, 12442 (2018)

11. X. Wang, A. Deng, W. Cao, Q. Li, L. Wang, J. Zhou, B. Hu, X.J. Xing, Mater. Sci. **53**, 6433 (2018)

12. S.Y. Gao, Y.G. Shi, S.X. Zhang, K. Jiang, S.X. Yang, Z.D. Li, E. Takayama-Muromachi, J. Phys. Chem. C. **112**, 10398–10401 (2008)

13. J. Santoyo-Salazar, M.A. Castellanos-Roman, L. Beatriz Gómez, Mater. Sci. Eng. C. **27**, 1317–1320 (2007)

14. M.D. Shultz, J.U. Reveles, S.N. Khanna, E.E. Carpenter, J. Am. Chem. Soc. **129**, 2482 (2007)

15. P.S. Haddad, T.M. Martins, L. D'Souza-Li, L.M. Li, K. Metze, R.L. Adam, M. Knobel, D. Zanchet, Mater. Sci. Eng. C. **28**, 489–494 (2008)

16. K. Park, G. Liang, X. Ji, Z.P. Luo, C. Li, M.C. Croft, J.T. Markert, J. Phys. Chem. C. **111**, 18512–18519 (2007)

17. M. Bonini, A. Wiedenmann, P. Baglioni, Mater. Sci. Eng. C. **26**, 745–750 (2006)

18. M. Stjerndahl, M. Andersson, H.E. Hall, D.M. Pajerowski, M.W. Meisel, R.S. Duran, Langmuir **24**, 3532–3536 (2008)

19. M.E. Khosroshahi, L. Ghazanfari, Physica E. **42**, 1824–1829 (2010)

20. Y. Kobayashi, S. Saeki, M. Yoshida, D. Nagao, M. Konno, J. Sol-Gel Sci. Technol. **45**, 35–41 (2008)

21. D. Yang, J. Hu, S. Fu, J. Phys. Chem. C. **113**, 7646–7651 (2009)

22. Z. Bo, X.J. Min, L.Y. Qi, L.H. Zhou, Sci China Ser B-Chem. **51**, 145 (2008)

23. T.Z. Yang, C.M. Shen, H.J. Gao, J. Phys. Chem. B. **109**, 23233–32323 (2005)

24. H.C. Lu, I.S. Tsai, Y.H. Lin, J. Physics: Conf. Series. **188**, 012039 (2009)

25. C.A. Mirkin, MRS Bull **25**, 43–54 (2000)

26. J.M. Lehn, Angew. Chem. Int. Ed. Engl. **29**, 1304–1319 (1990)

27. M.J. Rosen, *Handbook* (Wiley-Interscience, NJ, 2004)

28. V.A. Basyuk, A.A. Chuico, Zh. Prikl, Spektrosk. **52**, 935 (1990)

29. R.A. Williams, H.W. Blanch, Biosens. Bioelectron **9**, 159–167 (1994)

30. R.K. Dey, T. Patnaik, V.K. Singh, S.K. Swain, C. Airoldi, Appl. Surf. Sci. **255**, 8176–8182 (2009)

31. X. Zhang, W. Wu, J. Wang, X. Tian, Appl. Surf. Sci. **254**, 2893–2899 (2008)

32. M.A. Hernandez, R.J. Martın-Palma, J.P. Rigueiro, J.P.G. Ruiz, J.L.G. Fierro, J.M.M. Duart, Mater. Sci. Eng. C. **23**, 697–701 (2003)

33. H. Cao, J. He, L. Deng, X. Gao, Appl. Surf. Sci. **255**, 7974–7980 (2009)

34. P. Oberacker, P. Stepper, D.M. Bond, S. Höhn, J. Focken, V. Meyer, L. Schelle, V.J. Sugrue, G.J. Jeunen, T. Moser, S.R. Hore, F. vonMeyenn, K. Hipp, T.A. Hore, T.P. Jurkowski, PLOS Biol. **17**, e3000107 (2019)

35. S. Kralj, D. Makovec, S. Čampelj, M. Drofenik, J. Magn. Magn. Mater. **322**, 1847–1853 (2010)

36. C. Lee, Y.W. Kwon, J.I. Jin. (Mater. Sci. DNA, CRC Press, 2011), pp. 121–162

37. C. Hui, C. Shen, J. Tian, L. Bao, H. Ding, C. Li, Y. Tian, X. Shi, H.J. Gao, Nanoscale **3**, 701–705 (2011)

38. H. Husain, B. Hariyanto, M. Sulthonul, W. Klysubun, D. Darminto, S. Pratapa, Mater. Res. Express. **6**, 086117 (2019)

39. H.P. Klug, L.E. Alexander, *X-ray Diffraction Procedures for Polycrystalline and Amorphous Materials* (John Wiley & Sons, New York, 1962)

40. K. Amemiya, A. Toyoshima, T. Kikuchi, T, Kosuge, K. Nigorikawa, R. Sumii, K. Ito, AIP Conf. Proc. **1234**, 295–298 (2010)

41. J.S. Lee, Y. Xie, H. Sato, C. Bell, Y. Hikita, H.Y. Hwang, C.-C. Kao, Nature Mater. **12**, 703–706 (2013)

42. R.M. Cornell, U. Schwertmann. *The Iron Oxides: Structure*. Properties. Reactions. Occurrence and Uses, 2nd edn, (Wiley-VCH Verlag GmbH & Co. KgaA, Weinheim, 2003)

43. A.G.S. Prado, E.A. Faria, P.M. Padilha, Quim. Nova. **28**, 544 (2005)

44. C.R. Deltcheff, M. Amirouche, M. Fournier, J. Catal. **138**, 445 (1992)

45. M. Esmaeilpour, J. Javidi, F.N. Dodeji, M.M. Abarghoui, J. Mol. Catal. A. **393**, 18 (2014)

46. H.L. Ding, Y.X. Zhang, S. Wang, J.M. Xu, S.C. Xu, G.H. Li, Chem. Mater. **24**, 4572–4580 (2012)

47. A. Hashemzadeh, M.M. Amini, R. Tayebee, A. Sadeghian, L.J. Durndell, M.A. Isaacs, A. Osatiashtiani, C.M.A. Parlett, A.F. Lee, Mol. Catal. **440**, 96–106 (2017)

48. F.H. Aragon, P.E.N. deSouza, J.A.H. Coaquira, P. Hidalgo, D. Gouvea, Physica B. **407**, 2601 (2012)

49. W.D. Callister, *Materials Science and Engineering: An Introduction* (Wiley, New York, 2007)

50. J. Stöhr, S.H. Ciegmann, *Magnetism: from Fundamentals to Nanoscale Dynamics* (Springer, Berlin; New York, 2006)

51. D. Mauri, D. Scholl, H.C. Siegmannand, E. Kay, Phys. Rev. Lett. **61**, 758–761 (1988)

52. X. Zhao, Y. Shi, T. Wang, Y. Cai, G. Jiang, J. of Chromatography A **1188**, 140–147 (2008)

53. M. Coskun, M. Korkmaz, J. Nanopart, Res. **16**(2316), 1–12 (2014)

54. S. Ayyappan, S.P. Raja, C. Venkateswaran, J. Philip, B. Raj, Applied Physics. Lett. **96**, 143106 (2010)

55. C.T. Chen, Y.U. Idzerda, H.J. Lin, N.V. Smith, G. Meigs, E. Chaban, G.H. Ho, E. Pellegrin, F. Sette, Phys. Rev. Lett. **75**, 152–155 (1995)

56. T.J. Regan, H. Ohldag, C. Stamm, F. Nolting, J. Luning, J. Stohr, R.L. White, Phys. Rev. B. **64**, 214422 (2001)

57. E. Pellegrain, M. Hagelstein, S. Doyle, H.O. Moser, J. Fuchs, D. Vollath, S. Schuppler, M.A. James, S.S. Saxena, L. Niesen, O. Rogojanu, G.A. Sawatzky, C. Ferrero, M. Borowski, O. Tjernberg, Phys. Status Solidi B. **215**, 797–801 (1999)

58. C.H. Ho, C.P. Tsai, C.C. Chung, C.Y. Tsai, F.R. Chen, H.J. Lin, C.H. Lai, Chem. Matter. **23**, 1753–1760 (2011)

59. R. Nongjai, R. Samad, V.R. Singh, V.K. Verma, A. Kandasami, J. of Mag. and Mag. Mats. **527**, 167703 (2021)

60. P. Kumari, M. Zzaman, S. Jena, M. Kumar, R.R. Bharadwaj, V.K. Verma, R. Shahid, K. Amemiya, V.R. Singh, J. Supercond. and Nov. Magn. **34**, 1119 (2021)

61. V.R. Singh, Y. Sakamoto, T. Kataoka, Y. Yamazaki, A. Fujimori, F.H. Chang, D.J. Huang, H.J. Lin, C.T. Chen, Y. Yamada, T. Fukumura, M. Kawasaki, J. of Phys.: Cond. Mat. **23**, 176001 (2011)

62. Y. Yamazaki, T. Kataoka, V.R. Singh, A. Fujimori, F.H. Chang, D.J. Huang, H.J. Lin, C.T. Chen, K. Ishikawa, K. Zhang, S. Kuroda, J. of Phys.: Cond. Mat. **23**, 176002 (2011)

63. V.R. Singh, V.K. Verma, K. Ishigami, G. Shibata, A. Fujimori, T. Koide, M. Shirai Y. Miura, T. Ishikawa, G.F. Li, M. Yamamoto, J. Appl. Phys. **117**, 203901 (2015)

64. R. Dawn, M. Zzaman, R.R. Bharadwaj, C. Kiran, R. Shahid, V.K. Verma, S.K. Sahoo, K. Amemiya, V.R. Singh, J. of Sol-Gel Sc. & Tech. **99**, 461–468 (2021)

65. M. Kumar, V.K. Verma, V.R. Singh, Surface Interface Analysis **53**, 808–813 (2021)

66. S. Jena, M. Zzaman, V.K. Verma, K. Ishigami, G. Shibata, M. Yamamoto, R. Shahid, T. Koide, A. Fujimori, V.R. Singh, Physica B: Phys. of Con. Matt. **627**, 413619 (2022)

67. Y.P. Cai, K. Chesnel, M. Trevino, A. Westover, R.G. Harrison, J.M. Hancock, S. Turley, A. Scherz, A. Reid, B. Wu, C. Graves, T. Wang, T. Liu, H. Durr, J. Appl. Phys. **115**, 17B537 (2014)

68. T. Saitoh, A.E. Bocquet, T. Mizokawa, A. Fujimori, Phys. Rev. B **52**, 7934 (1995)

69. D.J. Huang, C.F. Chang, H.-T. Jeng, G.Y. Guo, H.-J. Lin, W.B. Wu, H.C. Ku, A. Fujimori, Y. Takahashi, C.T. Chen, Phys. Rev. Lett. **93**, 077204 (2004)

70. X. Che, H.N. Bertram, J. of Magnetism and Magnetic Mater. **116**, 121–127 (1992)

71. E.S.D.T. de Mendonçaa, A.C.B. de Fariaa, S.C.L. Diasa, F.F.H. Aragónb, J.C. Mantillab, J.A.H. Coaquirab, J.A. Diasa, Surfaces and Interfaces **14**, 34 (2019)

72. K. Amemiya, Phys. Chem. Chem. Phys. **14**, 10477–10484 (2012)

73. B. Gilbert, J.E. Katz, J.D. Denlinger, Y. Yin, R. Falcone, G.A. Waychunas, J. Phys. Chem. C. **114**, 21994 (2010)

74. F.M.F. deGroot, M. Grioni, J.C. Fuggle, J. Ghijsen, G.A. Sawatzky, H. Petersen, Phys. Rev. B. **40**, 5715 (1989)

75. S. Giovannini, F. Boscherini, R. Carboni, L. Signorini, L. Pasquini, N. Mahne, A. Giglia, M. Pedio, S. Nannarone, M. Benfatto, S.D. Longa, D. Longa, Phys. Scr. T. **115**, 424 (2005)

76. M. Pollak, M. Gautier, N. Thromat, S. Gota, W.C. Mackrodt, V.R. Saunders, Nucl. Instrum. Meth. Phys. Res. Sect. B. **97**, 383 (1995)